KSME

Springer

Journal of Mechanical Science and Technology 34 (7) 2020

Original Article
DOI 10.1007/s12206-020-0618-1

Keywords:
· Dynamic stall
· Turbulence
· Particle image velocimetry
· Flow structure
· POD

Correspondence to:
Kyung Chun Kim
kckim@pusan.ac.kr

Citation:
Chang, G., Karbasian, H. R., Zhang, S., Yan, Y., Chen, B., Kim, K. C. (2020). The influence of kinematics of blades on the flow structure in deep dynamic stall. Journal of Mechanical Science and Technology 34 (7) (2020) 2855~2868. http://doi.org/10.1007/s12206-020-0618-1

Received December 5th, 2019
Revised April 8th, 2020
Accepted April 15th, 2020

† Recommended by Editor Yang Na

The influence of kinematics of blades on the flow structure in deep dynamic stall

Gul Chang[1,2], Hamid Reza Karbasian[1], Shujun Zhang[3], Yao Yan[4], Binqi Chen[4] and Kyung Chun Kim[1]

[1]School of Mechanical Engineering, Pusan National University, Busan 46241, Korea, [2]RAC Business Unit, LG Electronics, Inc., Changwon 642-711, Korea, [3]Computational Aerodynamics Institute, China Aerodynamics Research and Development Center, Mianyang 621000, China, [4]School of Aeronautics and Astronautics, University of Electronics Science and Technology of China, Chengdu, China

Abstract This study considers the effect of kinematics on the aerodynamic loads and flow structure around moving blades of micro air vehicles (MAVs) in deep dynamic stall. The transversal (pure heaving) and rotational (pure pitching) motions are considered distinctly to investigate the dynamic stall. An equivalent effective angle of the attack profile is given to both motions. This method helps to figure out the influence of kinematics on flow structures when all boundary conditions and effective angles of attack profiles are the same. An experiment is conducted in fully turbulent flow at Re = 1.5×10^4 to avoid any transition regime in the boundary layer, and make the results relatively independent of the flow characteristics. A NACA 0012 airfoil is chosen at high reduced frequencies (k = 0.25 and 0.375) and high angles of attack to reach deep dynamic stall conditions. Additionally, time-resolved particle image velocimetry (PIV) and post-processing are used to compute the aerodynamic loads using a control-volume approach. The flow field is also reconstructed using proper orthogonal decomposition (POD) to separate the flow structures in different modes. It is shown that the kinematics can significantly influence the flow structure and aerodynamic loads. In the pre-stall region, the pure pitching motion usually produces higher lift force, while the pure heaving motion has a higher lift peak. However, in the post-stall region, the pure heaving motion usually has higher lift than the pure pitching motion. The pure heaving motion produced lower drag force than the pure pitching motion. For pure heaving motion, the POD analysis reveals there is a high-energy mode in the flow structure that helps to make the vortices more stable compared to pure pitching motion. Furthermore, the pure heaving motion adds extra kinetic energy to the boundary layer, which decelerates the reversal flow and the transfer of the separation point on suction side of the airfoil.

1. Introduction

Dynamic stall is one of the important phenomena in unsteady aerodynamics, especially in the micro air vehicles (MAV). Dynamic stall is associated with the dynamics of the blades/wings, which show large hysteresis in aerodynamic loads. Compared to static stall, dynamic stall normally occurs at a higher angle of attack, which affects the aerodynamic behavior of the blades/wings [1-3]. Dynamic stall can result from any variation in the blade motion or flow pattern. For example, in the case of MAV, unsteadiness in the flow velocity or direction and thus dynamic stall can result from yawing, the wake from upstream rotor blades/wings, or large-scale turbulence [1]. Other significant reasons for dynamic stall are oscillation of the blades/wings, and changes in their pitch angle (for controlling power loads) [4, 5].

Hirano et al. [6] experimentally investigated dynamic stall behavior by smoke visualization. They indicated that the locations of the flow separation for a moving foil and hence the load variations can vary, in contrast to a static foil, where the flow reversal and separation mostly occur at a constant location. Dynamic stall is unavoidable in rotating blades. Dynamic stall has been studied extensively for pure pitching foils [3, 7-14]. A mushroom-like wake structure

occurs at low reduced frequencies (typically k < 0.2) due to the initiation, formation, and shedding of the leading edge vortex (LEV) and its interaction with trailing edge vortex (TEV) [14]. At higher reduced frequencies, the interaction between LEV and TEV changes and produces a jet-like wake structure, which is representative of inverse von-Karman streets [15]. Jones et al. [16] numerically and experimentally investigated the pure heaving motion and found jet-like wake structure at sufficiently high pure heaving velocities. Young and Lai [17] numerically investigated the pure heaving motion of NACA 0012 foils over a range of reduced frequencies and pure heaving amplitudes, which significantly impact the aerodynamic features in dynamic stall.

Lift and thrust can be enhanced by a combination of pure heaving and pure pitching with a specific difference in phase angle between the pure heaving and pure pitching motions [18-27]. This difference in phase angle also has a great effect on propulsion performance [19]. Ashraf et al. [20] numerically investigated the effect of the thickness and camber of a pure heaving and pure pitching airfoil's over the range of Re = 200-20000. Karbasian et al. [22] numerically investigated the performance of a pure heaving/pure pitching airfoil with different kinematics. They found that the kinematics of a flapping airfoil has a significant impact on the propulsion performance, and it can be applied to improve power extraction using flapping energy convertors [28].

The kinematics can influence the flow pattern and vortex structure and lead to aerodynamic changes in equivalent conditions. This study examines both pure heaving and pure pitching motions in order to see what the effect of kinematics is on the flow structure and hence, aerodynamic loads. An analogous effective angle of attack profile was specified, and motion characteristics of pure heaving and pure pitching motions are set to have equivalent profiles of the angle of attack. The kinematics of these motions was examined using the same conditions to determine the influence of kinematics on dynamic stall. For this purpose, the flow field in deep dynamic stall was quantitatively visualized using particle image velocimetry (PIV).

2. Physical model

Dynamic stall in MAVs can result from transversal vibration of the blades, pure pitching, yawing, variations in fluid velocity and even dynamic behavior of the blades/wings [4, 5]. Considering different types of kinematics could provide detailed information on the flow structures, loads and flow control to prevent undesirable phenomena. In pure pitching motion, the airfoil rotates around a pivot point (or axis), and the angle between incident flow and chord line changes continuously. In pure heaving motion, the airfoil has transversal motion, which can perturb flow behind the airfoil. The direction of this motion with respect to the free stream flow creates an angle between the overall flow direction and the chord line. The kinematic motions are shown in Fig. 1. According to Fig. 1(a), the pure pitching motion of a blade occurs around the main axis (the z coordinate) connected to the hub. In MAVs, this motion is used to control the propulsion at different speeds. Due to the elasticity of the MAV's blades/wings, the blades start to fluctuate (usually in y direction). The continuous bending of blades leads to reciprocal motions along the y direction. As shown in Fig. 1(b), the pure pitching motion forms an unsteady angle β with the free stream velocity, U_0, and the mean angle of attack is α_0. The combination of these two angles determines the effective angle of attack, α. In Fig. 1(c), the airfoil has pure heaving motion (up/down motion in the y direction) with pure heaving velocity denoted by dh. The pure heaving velocity and free stream velocity components also form a variable angle, β, which determines the effective angle of attack, α, along with the mean angle of attack.

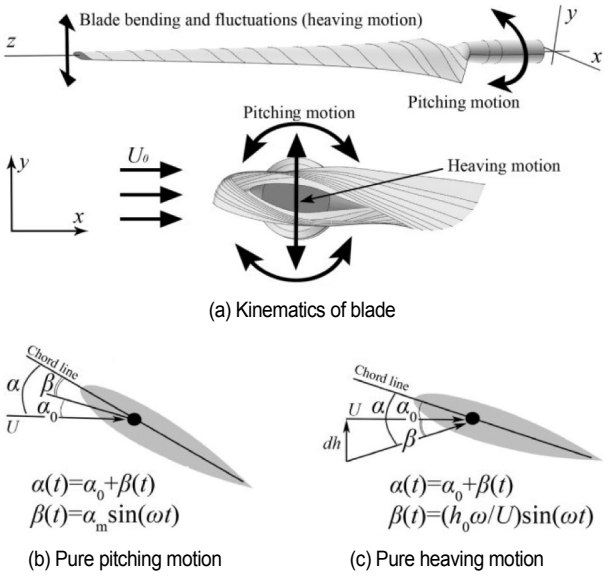

Fig. 1. Schematic of pure pitching and pure heaving motions, and their related angle of attack function.

The pure pitching motion of the airfoil introduces a sinusoidal effective angle of attack, α_p, as a function of time:

$$\alpha_p(t) = \alpha_0 + \beta(t)$$
$$\beta(t) = \alpha_m \sin(\omega t) \quad (1)$$

where α_m, f, and t are pitch amplitude, oscillating frequency and operating time, respectively. The oscillation frequency can be determined by the reduced frequency k:

$$k = \frac{\pi f c}{U} \quad (2)$$

where c is the chord length of the airfoil. The reduced frequency represents the ratio of the convective time scale and the forced oscillation time scale [29].

In the case of pure heaving motion, transversal motion of the airfoil with a constant initial angle forms an angle with the free stream velocity and determines the effective angle of attack. Based on the kinematics of the pure heaving airfoil, the motion equation can be calculated as follows:

$$h(t) = h_m \sin(\omega t) \tag{3}$$

where h_m is the pure heaving amplitude. This motion equation can introduce a new form of effective angle of attack for pure heaving motion, and it represents the angle of incident flow with the airfoil's chord line as follows:

$$\alpha_h(t) = \alpha_0 + \beta(t)$$
$$\beta(t) = \tan^{-1}\left[\frac{\omega h_m}{U_0}\cos(\omega t)\right]. \tag{4}$$

Two distinct kinematic motions with different features are introduced. In this study, the airfoil has two distinct kinematic motions with the same effective angle of attack profile ($\alpha_p = \alpha_h$). When all relative motions are the same for pure heaving and pure pitching motions, the aerodynamic loads and flow structures may change. Any difference between the results of pure pitching and pure heaving motions can be attributed to a new concept regarding the influence of kinematics on the flow structures. This allows us to consider the effects of kinematic motions on the aerodynamics of airfoil in deep dynamic stall.

3. Experimental setup

3.1 Test tunnel

To perform the experiment it is decided to develop experimental setup and measure flow in wind tunnel. A 7.5-kW wind tunnel with a rectangular test section was used for the experiment. The test section is 0.4 m high and 0.4 m wide. A set of honeycombs and a stainless-steel screen were used in the settling chamber prior to test section to reduce turbulence intensity and provide a uniform flow distribution in the test section. The free stream velocity was set to 2 m/s with turbulence intensity less than 0.5 %. According to Kim and Xie [1], the free stream turbulence has a more significant effect on aerodynamic loads in comparison to laminar free stream flow. Therefore, a turbulence generator was also installed upstream, where the measured turbulence intensity was 3 %. However, significant measurement errors can occur if the flow is laminar or has low turbulence intensity due to any external effect or dynamic motions at high reduced frequencies (such as the kinematics, surface roughness, endplates, and so on). When the laminar flow reaches the airfoil surface, regimes of laminar, transition, and turbulent flow occur in the boundary layer. Therefore, any small disorder may change the location of the transition or separation points. The advantage of having upstream turbulent flow is that there is no concern about the transition regime in the boundary layer over the suction side of the airfoil. On the other hand, an airfoil subjected to free stream turbulence is less dependent on the Reynolds number than one subjected to smooth and laminar flow [1]. This also helps us to explain the results for flows with higher Reynolds numbers. Therefore, installing this turbulence generator assures that the flow is fully turbulent with a specified intensity.

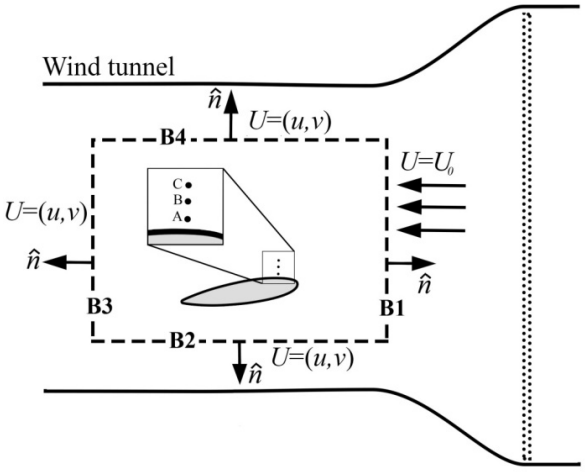

Fig. 2. Small wind tunnel used for the experimental study.

The airfoil considered is a NACA 0012 with a chord length (c) of 0.07 m and aspect ratio of 2. End plates are used to eliminate the free-surface and wall effects on the flow over the airfoil. This also assures that the span-wise flow would be negligible. Fig. 2 shows the wind tunnel and airfoil installed in the test section. A rectangular control volume bounds the airfoil with control surfaces B1, B2, B3 and B4. The boundary conditions are shown for each control surface. U is the fluid velocity with two components u and v. Upstream, the flow is uniform with the same velocity as the free stream velocity in the test section, U_0. $\hat{n}$ is a unit vector that is perpendicular to the control surface. Points A, B, and C in the control volume are aligned vertically near the leading edge of the airfoil. These points are the locations of the flow measurements (turbulence and kinetic energy). The stream-wise location of A, B, and C is 10 % of c (7 mm) from the leading edge and wall normal distance of A, B, and C is 1 mm, 4 mm, and 7 mm, respectively, from the airfoil surface.

3.2 Mechanisms and motion control

The mechanism used for creating the different kinematics is illustrated in Fig. 3. Fig. 3(a) shows the mechanism used for the pure pitching motion, in which the airfoil is joined to a stationary axis (pivot point), around which the airfoil can freely oscillate. A wheel rotates with a simple mechanism to convert the rotational motion to reciprocal motion. The reciprocal motion is transferred to the airfoil by joint 3, and it yields the rotation of airfoil. Therefore, the airfoil oscillates around the free pivot point and produces a desired angle with respect to the free stream (the effective angle of attack). The desired

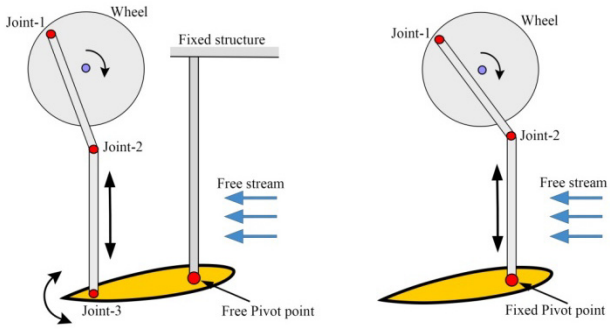

(a) Pitching motion (b) Heaving motion

Fig. 3. Schematic of motion control in the experimental setup for both pure pitching and pure heaving.

amplitude for the angle of attack is achievable by changing the distance between joint 1 and the center of the wheel. In Fig. 3(b), the airfoil has pure heaving motion. The wheel rotates, and the rotational motion is converted again to reciprocal motion. In this case, the pivot point is fixed, and the airfoil cannot oscillate around the pivot point. Therefore, the airfoil has transversal motion, and it produces an angle with the free stream velocity. Again, the amplitude of the motion can be adjusted using joint 1.

3.3 Particle image velocimetry (PIV)

A typical PIV system consists of 1) a set of tracer particles with appropriate size and density to trace the flow; 2) a laser source for illuminating the tracer particles; 3) an optical lens for converting the laser beam into a laser sheet; 4) a CCD or CMOS camera to capture images; and 5) post-processing code for image processing and flow analysis. In the PIV experiment, the air is seeded with micro particles of olive oil with diameters of approximately 2 μm. The time-resolved planar PIV with a two-dimensional (2D) laser sheet were used. The laser source was a continuous-wave diode laser with maximum power of 3 W and wavelength of 532 nm. The thickness of the laser sheet in the location of interest is approximately 1 mm. Images were captured with a monochrome CMOS camera (Photron FASTCAM SA 1.1) with observation area of 11 cm × 11 cm. The resolution of captured images is 1024×1024 pixels, and the quality of pixels is 12 bits. For data acquisition, the frame rate of the camera was set to 1000 to 5000 fps. Errors were sufficiently low in the velocity vector results at 3000 fps, so all experiments were done using this rate. The size of the interrogation cell was selected as 26×26 pixels with 50 % overlapping, which satisfies the Nyquist sampling criterion. Fig. 4 shows the experimental setup used to visualize the flow field around a moving airfoil. As shown in Fig. 4(a), the CMOS camera is installed outside of the test section, and a continuous wave laser sheet illuminates the center of the test section from underneath. The kinematic setup of the airfoil is implemented on top of the test section. As shown in Fig. 4(b), the airfoil can move with help of vertical bars that link the airfoil to the kinematic setup. Fig. 4(c) shows the PIV field of view with the airfoil.

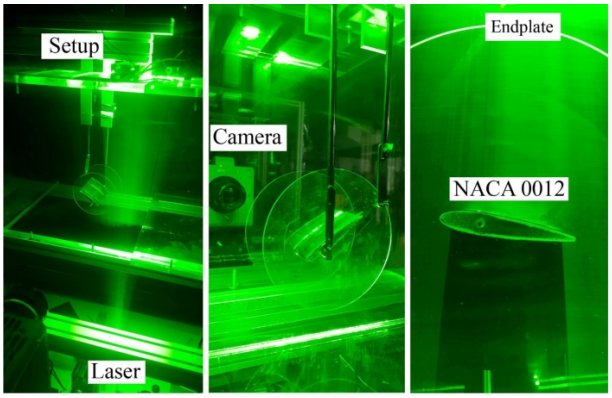

(a) (b) (c)

Fig. 4. Experimental setup: A PIV system is installed outside of a wind tunnel, and the setup moves the airfoil inside the test section.

The PIV measurements were made at the center plane of the airfoil model, while the structures for pitching and heaving motions are located side area from the two-dimensional model. Interactions between the structure and flow can be possible at the side wall of test section, but the disturbances cannot be reached to the center plane where the PIV measurements are made. Two endplates were installed at both sides of the airfoil to reduce the three-dimensional effects and remove the tip vortex effects on the flow structure. All results were captured in the middle of the wing to reduce blockage effect on the results.

3.4 Force measurement using PIV results

The aerodynamic loads on the airfoil can be determined based on the linear momentum by integrating the flow variables along the control surfaces, as shown in Fig. 2. The momentum exerted on the airfoil can be calculated as follows:

$$F = -\iiint_V \frac{d}{dt}(\rho U)\,dV - \iint_S \rho U(U.\hat{n})ds - \iint_S P\hat{n}ds + \iint_S (\tau.\hat{n})ds \tag{5}$$

where P and τ are the pressure and viscous stress tensor, respectively. The effects of unsteady terms on the aerodynamic loads are negligible at lower reduced frequencies [30, 31]. But this study considers turbulent flow and relatively high reduced frequencies, so it is important to consider the unsteady terms. The 2D domain bounded by a fixed control volume is considered. Thus, the equations for aerodynamic loads can be converted as follows:

$$L = \rho\oint[-uvdy + vvdx] + \oint Pdx + \mu\oint\left[-2\frac{\partial v}{\partial y}dx + \left(\frac{\partial u}{\partial y} + \frac{\partial v}{\partial x}\right)dy\right] + \oint\left[-\overline{u'v'}dy + \overline{v'v'}dx\right] \tag{6}$$

$$D = \rho\oint[-uudy + uvdx] - \oint Pdy + \mu\oint\left[2\frac{\partial u}{\partial x}dy - \left(\frac{\partial u}{\partial y} + \frac{\partial v}{\partial x}\right)dx\right] + \oint\left[-\overline{u'u'}dy + \overline{u'v'}dx\right] \quad (7)$$

where L and D are the lift and drag forces, respectively. The aerodynamic loads are reported based on the non-dimensional forms of the lift and drag coefficients:

$$C_L, C_D = \frac{[L, D]}{0.5\rho c U^2} \quad (8)$$

The pressure term along the surface control was computed using the Poisson equation for simplicity. Based on Eqs. (6) and (7), the velocity, pressure, and unsteady terms were integrated throughout the control surface. For a static airfoil, some corrections were introduced by van Oudheusden et al. to reduce the drag errors [32]. In the present study, the airfoil is dynamic, and the drag force measurement is challenging due to the errors for strong vortices with high velocity, which introduce high uncertainties in the pressure and wake area. To minimize the error for drag measurement in the dynamic case, the control surface was placed far enough from the TEV [33].

The vertical control surface near the suction side of the airfoil is not very close to the leading edge or airfoil surface. The level of image noise in that area is high due to light refraction in the suction wall of the airfoil. When the laser sheet illuminates the flow, a shadow on the pressure side of the airfoil appears. Fig. 2 shows that some parts of control surface B2 are located in the shadow, for which no velocity data is available. However, the variations of the velocity along the control surface B2 are negligible if the control surface is kept far enough away from the airfoil. Therefore, the velocity profile along the B2 can be estimated with a simple interpolation.

In the case of load computations, each case was tested ten times to assure the accuracy of results. Furthermore, five different control volumes were selected to compute the aerodynamic loads. As shown in Fig. 2, the location of B1 was constant, while B2, B3 and B4 were moved to 0.5c away from the airfoil (except for B2, where the maximum distance was c). Therefore, fifty different results were examined for each specified moment, and then, the range of uncertainties was computed. Finally, all the results were averaged for both the lift and drag forces and presented with uncertainty bars in upcoming section.

4. Results and discussion

4.1 Aerodynamic loads

Table 1 provides four different cases with different effective angle of attack profiles and reduced frequencies. The instantaneous aerodynamic loads (lift and drag coefficients) were examined and compared for each case. All angles are shown as α since the effective angle of attack profile in this study is equivalent for both pure heaving and pure pitching motions. Fig. 5(a) shows the lift coefficient for case 1. The angle of attack varies between 0° and 20°, and the reduced frequency is k = 0.25. The lift coefficient increases gradually until α = 15°, and then its slope increases abruptly because of LEV formation. This sharp change in the lift coefficient has been observed previously [9, 10, 34]. The angle of attack increases and reaches its maximum value, where the maximum lift coefficient occurs at this point. Stall also occurs at this moment [1, 4, 10], and the LEV covers most of the suction side of the airfoil. With decreasing of the angle of attack, the lift coefficient drops suddenly due to pinch-off. In the post-stall region, the aerodynamic loads are more unstable due to the complex flow structures, which lead to fluctuation in the lift coefficient. Measuring the forces in this region is still challenging and needs more effort.

Fig. 5(b) illustrates the instantaneous drag coefficient for case 1. The drag coefficient becomes slightly negative at lower angles in the pre-stall region. This occurs because the small vortices at this reduced frequency shed into the wake and turn into inverse von-Karman streets for a short period. The vortex structure changes, and then it creates a slight jet flow behind

Table 1. Case studies with different effective angle of attack profiles and reduced frequencies.

Case	Effective angle of attack	K
Case 1	$\alpha = 10°+10°\sin(\omega t)$	0.25
Case 2	$\alpha = 20°+10°\sin(\omega t)$	0.25
Case 3	$\alpha = 10°+15°\sin(\omega t)$	0.375
Case 4	$\alpha = 20°+15°\sin(\omega t)$	0.375

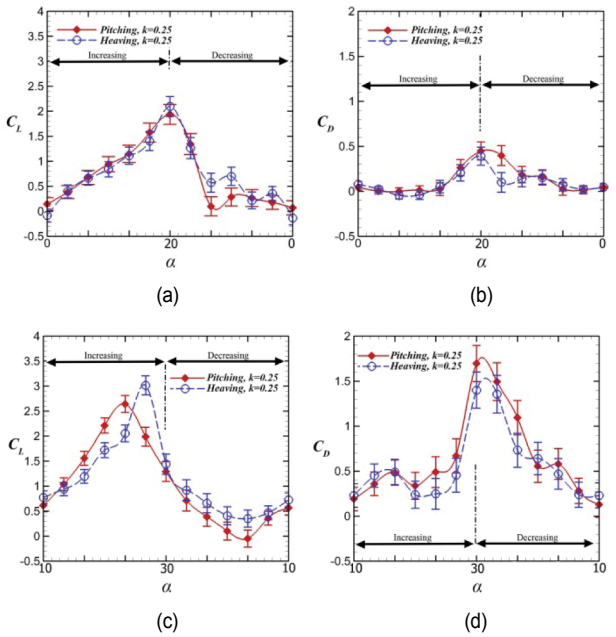

Fig. 5. Instantaneous aerodynamic loads in one oscillating cycle: (a) Lift coefficient for case 1; (b) drag coefficient for case 1; (c) lift coefficient for case 2; (d) drag coefficient for case 2.

the airfoil along with thrust. When increasing the angle of attack, the separation point advances toward the leading edge. Due to the adverse pressure gradient near the leading edge, a large separation bubble is formed. With further increasing of the angle of attack, the separation bubble turns into a LEV, and this increases the drag force. The maximum drag force could occur right after stall or in the pre-stall region, where the TEV starts to develop. The drag coefficients for both pure heaving and pure pitching motions reach their peak after the stall, and they decrease with decreasing of the angle of attack. Additionally, the drag force produced by the pure pitching motion is notably higher than that of pure heaving motion in the post-stall region.

Fig. 5(c) shows the lift coefficient for case 2. In this case, the angle of attack varies between 10° and 30°, and the reduced frequency is k = 0.25 as well. The lift coefficient for both pure heaving and pure pitching motions are the same at α = 10°. Later, the lift coefficient for pure pitching starts to increase more than that of the pure heaving motion. In other words, the pure pitching motion produces higher lift than the pure heaving motion in the pre-stall region. This occurs because the flow reversal happens earlier in pure pitching motion than in pure heaving motion. Therefore, in pre-stall region, it is expected that the separation point advances toward the leading edge, and it increase the lift coefficient for pure pitching motion. With increasing the angle of attack, the LEV is formed, and this LEV changes the slope of the lift coefficients. In the case 2, no changes can be observed in the slope for pure pitching motion. The pure pitching foil reaches the stall point at α = 24.6°, where the maximum lift coefficient occurs. However, the lift coefficient for pure heaving motion increases until α = 27.5°. This delay in stall occurs because of delay in progress of the separation point. The lift coefficient at the stall point (with the maximum lift coefficient) is higher for pure heaving motion than pure pitching motion. Additionally, the lift coefficient in the post-stall region is mostly higher than that of pure pitching motion.

Fig. 5(d) shows the drag coefficient for case 2. The pure pitching airfoil mostly produces a higher drag coefficient than the pure heaving motion. The drag coefficient for both pure heaving and pure pitching motions reach its maximum values after the stall point, when the TEV develops. The small fluctuations in the pre-stall and post-stall regions might be due to small vortex shedding or the instabilities on the suction side of the airfoil at lower angles of attack.

Fig. 6(a) shows the lift coefficient for case 3. In this case, the angle of attack varies between -5° and 25°, and the reduced frequency is 0.375 as well. The lift coefficient increases gradually in the pre-stall region. In this region, the lift coefficient usually varies linearly at lower angles of attack, where the flow is not fully separated. As mentioned, the pure pitching motion results in earlier reversal flow, and it advances the separation point toward the leading edge. So it is expected to have higher aerodynamic loads. Therefore, the lift coefficient for pure pitching motion in the pre-stall region is higher than that of pure heaving motion. The LEV starts to grow at approximately α = 21°, and it develops even when the angle of attack starts to decrease. The pure pitching motion produces a higher lift coefficient at lower angles of attack in the pre-stall region, while the pure heaving motion has a higher lift value at the stall point and in the post-stall region (except at negative angles). In this case, the stall does not occur at the maximum angle of attack. The LEV even grows when the angle of attack starts to decrease. This illustrates fast motion of the airfoil leads to a delay in LEV formation. This could happen when excessive kinetic energy is added to the boundary layer, which decelerates the transformation of separation point and the reversal flow activities. Therefore, the boundary layer would be more stable, and the flow would tend to attach to the suction surface until instability occurs. That is why the LEV begins to develop later at higher frequencies when the angle of attack is decreasing. Therefore, the airfoils at higher reduced frequencies add excessive kinetic energy in the boundary layer, which accelerates the flow, and decreases the probability of flow separation.

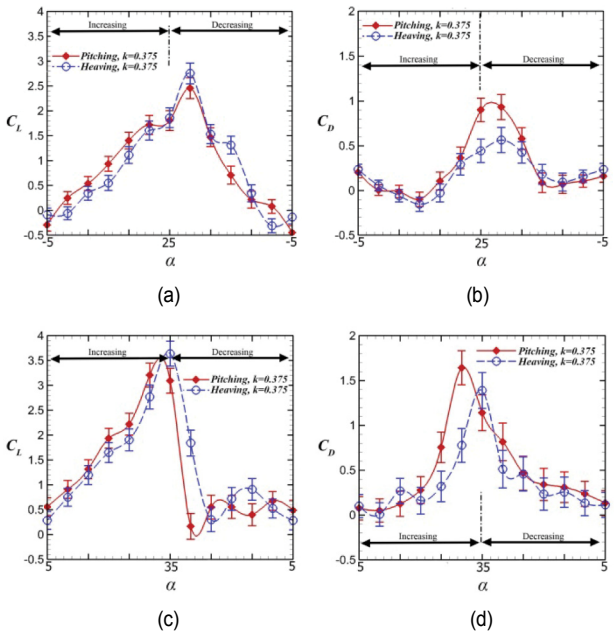

Fig. 6. Instantaneous aerodynamic loads in one oscillation cycle: (a) Lift coefficient for case 3; (b) drag coefficient for case 3; (c) lift coefficient for case 4; (d) drag coefficient for case 4.

Fig. 6(b) shows the instantaneous drag coefficient for case 3. With increasing of the angle of attack (positive angles), the vortices turn into inverse von-Karman streets, and create it thrust in this short period. With further increases in the angle of attack, the drag coefficient increases for both pure heaving and pure pitching motions right after the stall point. In the post-stall region, the drag coefficients drop as the angle of attack decreases. In this case, the drag coefficient for the pure pitching airfoil is mostly higher than that of pure heaving motion, and the differences become highly significant near the stall point.

Fig. 6(c) presents the lift coefficient for case 4, in which the angle of attack varies between 5° and 35° and the reduced frequency is k = 0.375 as well. The lift coefficient increases with

the angle of attack, and the lift for pure pitching motion is again higher than that of pure heaving motion in the pre-stall region. Because the reduced frequency is high, the airfoil motion adds additional energy to the boundary layer, and it decelerates the reversal flow on the suction side of the airfoil. Hence, the separation bubble formation occurs at higher angles of attack (α = 24° for pure pitching motion and α = 27.5° for pure heaving motion). Because the pure pitching motion advances the separation point earlier than the pure heaving motion, it reaches stall point earlier as well (α = 32°). Therefore, the pure heaving motion obviously has more delay in the stall (α = 35°) than the pure pitching motion. In the post-stall region, the pure heaving motion usually has a higher lift coefficient, but it seems to be more unstable with large fluctuation amplitude. The lift coefficient for pure pitching motion also has some fluctuations but with a small fluctuation amplitude. These fluctuations result from vortices, which develop and shed into the wake.

Fig. 6(d) illustrates the drag coefficients for case 4. The drag forces begin to increase with the angle of attack. Later, the drag coefficients reach their maxima right after the stall point for pure pitching motion, and at the stall point for pure heaving motion. When the TEV starts developing, the flow from the pressure side of the airfoil rushes to the suction side. Hence, the pressure near the trailing edge on the suction side of the airfoil increases. Therefore, it is expected that the lift force drops, and the flow separation occurs behind the airfoil. The LEV is a low-pressure vortex that notably decreases the pressure on the suction side of the airfoil. LEV pinch-off reduces the lift force, and causes a wide wake beyond the airfoil. Interestingly, the airfoil with pure pitching motion produces higher drag force than that with pure heaving motion. Small fluctuations in the post-stall region for pure heaving motion also occur because of small vortex shedding after the primary LEV and TEV.

4.2 Flow structure

Fig. 7 shows the vorticity contours superimposed with velocity vectors for case 1. As shown in Figs. 7(a) and (g), the angle of attack is α = 5° for both pure heaving and pure pitching motions. At this angle, the flow reversal occurs near the trailing edge for pure heaving motion (Fig. 7(a)), while for pure pitching motion, the Kelvin-Helmholtz instability occurs near the leading edge. This instability shows that the flow is unstable. When the angle of attack increases to α = 10°, the flow reversal near the trailing edge starts to grow for pure heaving motion, and the separation point advances toward the leading edge (Fig. 7(b)). For pure pitching motion at the same angle, the flow is separated, and the Kelvin-Helmholtz instability still occurs near the leading edge. At α = 15°, the shear layer near the leading edge becomes stronger for pure heaving motion, and a LEV is formed as well (Fig. 7(c)). For pure pitching motion at the same angle, the LEV is formed but it is smaller than that of pure heaving motion. This occurs because the shear layer for the pure heaving airfoil has more energy and feeds the LEV significantly. The pure pitching motion produces less energy in the

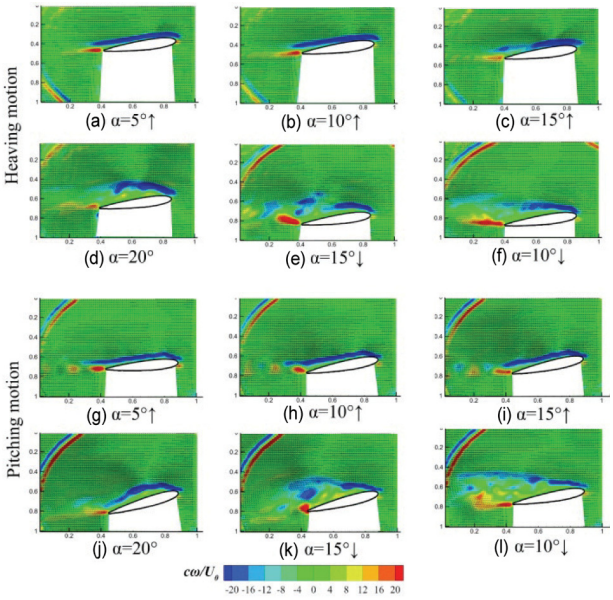

Fig. 7. Vorticity contours superimposed with velocity vectors at different angles of attack for case 1.

shear layer of the leading edge to feed the LEV. At the maximum angle of attack (α = 20°), the LEV covers the suction side of the airfoil for the pure heaving motion, and the lift coefficient reaches its maximum (Fig. 7(d)). For the pure pitching motion at the same angle, the LEV also covers the suction side but it seems to be smaller than that of the pure heaving motion. As it is mentioned, the pure heaving motion can provide a stronger shear layer near the leading edge to feed the LEV. Hence, upon injecting more energy to a vortex, it may grow in size and strength. When the angle of attack decreases to α = 15°, the TEV has already grown for pure heaving motion (Fig. 7(e)) but the TEV for pure pitching motion is still about to develop (Fig. 7(k)). Next, the LEVs for both pure heaving and pure pitching motions are separated from the suction side of the airfoil and shed to the wake. At this moment, an abrupt drop in the lift coefficient is expected. A secondary LEV is also created for both motions, which is about to move toward the trailing edge. With a further decrease in the angle of attack (α = 10°), the TEV leaves the airfoil and sheds to the wake for both motions. In this post-stall region, the flow is strongly separated, and other core vortices develop and leave the airfoil. Therefore, some fluctuations in the aerodynamic loads are expected for this region.

Fig. 8 shows the vorticity contours superimposed with velocity vectors for case 2. As the angle of attack increases to α = 15°, the LEV is fed by the shear layer at the leading edge of the airfoil and it begins to develop for both pure heaving and pure pitching motions (Figs. 8(a) and (g)). As the angle of attack reaches α = 20°, the LEV grows and becomes stronger for both pure heaving and pure pitching motions (Figs. 8(b) and (h)), and the lift coefficient increases notably. With a further increase to α = 25°, the LEV mostly covers the suction side of the pure heaving airfoil (Fig. 8(c)), and after this moment,

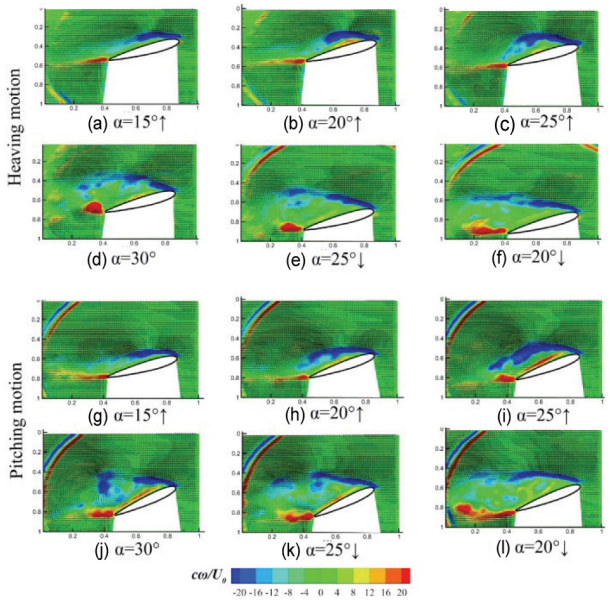

Fig. 8. Vorticity contours superimposed with velocity vectors at different angles of attack for case 2.

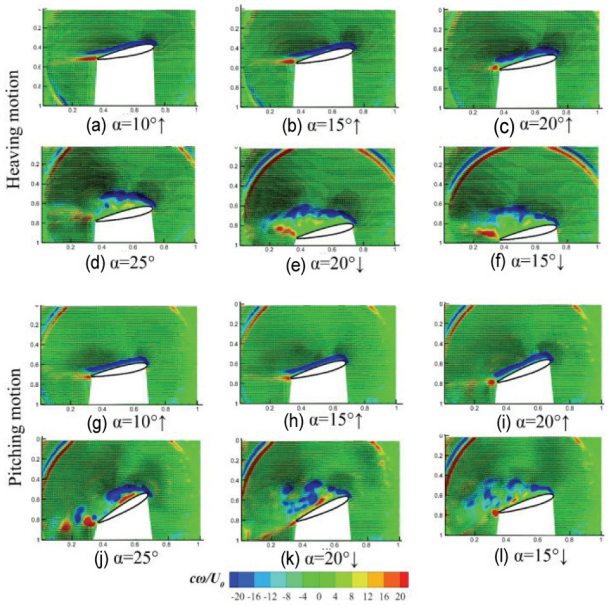

Fig. 9. Vorticity contours superimposed with velocity vectors at different angles of attack for case 3.

dynamic stall occurs. But for the pure pitching motion (Fig. 8(i)), the dynamic stall already occurred, and the LEV reaches its maximum lift force. The TEV also begins to develop for pure pitching motion, which indicates the LEV pinch-off, and hence, a reduction in lift force. As mentioned, the pure heaving motion results in less instability in the boundary layer on the suction side of the airfoil, which leads to a delay in the stall. At α = 30°, the LEV pinch-off already happened, and the TEV grows in size and strength (Figs. 8(d) and (j)). The TEV leads to a reduction in lift force, and it also increases the drag force in most cases [35]. Because stall occurs at the maximum angle of attack (α = 30°), the flow is strongly separated from the airfoil surface, and the drag coefficient increases continuously until the maximum angle of attack. With a decrease in the angle of attack to α = 25°, the lift and drag coefficients decrease. In this case, the flow still seems to be separated for both pure heaving and pure pitching motions (Figs. 8(e) and (k)), which continues until α = 20° (Figs. 8(f) and (l)).

Fig. 9 illustrates the vorticity contours superimposed with velocity vectors for case 3. For the pure heaving motion, the flow is attached to the airfoil with a small reversal flow near the trailing edge until α = 15° (Figs. 9(a) and (b)). Next, the separation bubble is formed near the leading edge of the airfoil due to the adverse pressure gradient (Fig. 9(c)). In the same case for pure pitching motion, flow reversal occurs near the trailing edge (Figs. 9(g) and (h)), and then at α = 20°, the separation bubble is formed near the leading edge as well (Fig. 9(i)). With a further increase in the angle of attack to α = 25°, the flow in case 3 seems to be more stable than cases 1 and 2, due to the higher reduced frequency. As shown in Fig. 9(d) for the pure heaving motion, the LEV develops in size and strength. In this condition, the LEV is still attached to the airfoil surface, and stall has not yet occurred even at the maximum angle of attack, α = 25°. For the pure pitching motion at the same angle (Fig. 9(j)), the LEV and aerodynamic loads are still growing. For both motions, these results show that higher reduced frequencies could delay the stall and increase the lift coefficient even after the maximum angle of attack. With a decrease in the angle of attack to α = 20°, the stall occurs for both pure heaving and pure pitching motions (Figs. 9(e) and (k)). At this moment, the LEV mostly covers the suction side of the airfoil, and the TEV begins to develop. With a further decrease in the angle of attack to α = 15°, the TEV begins to grow in size and strength, while the LEV detaches from the airfoil surface and sheds to the wake.

Fig. 10 illustrates the vorticity contours superimposed with velocity vectors for case 4. As the angle of attack increases to α = 20°, the flow separates near the trailing edge for pure heaving motion in the post-stall region, and there is no sign of separation bubble formation at this angle (Fig. 10(a)). For the pure pitching motion at the same angle, the flow reversal occurs near the trailing edge, and the LEV develops as well. This shows that the aerodynamic loads for pure pitching motion in the pre-stall region are much higher than those of pure heaving motion at the same angle. With a further increase in the angle of attack to α = 25° (Fig. 10(b)), the flow stays relatively stable for the pure heaving motion, and the LEV begins to grow at α = 30° (Fig. 10(c)). But for the pure pitching motion, the LEV continuously grows in size and strength until α = 30° (Figs. 10(h) and (i)), and it still produces a higher lift coefficient than the pure heaving motion at the same angle. At the maximum angle of attack, α = 35°, the LEV mostly covers the suction side of the airfoil, and dynamic stall is about to occur for both pure heaving and pure pitching motions (Figs. 10(d) and (j)). With a decreasing angle of attack in the post-stall region to α = 30°, the trailing

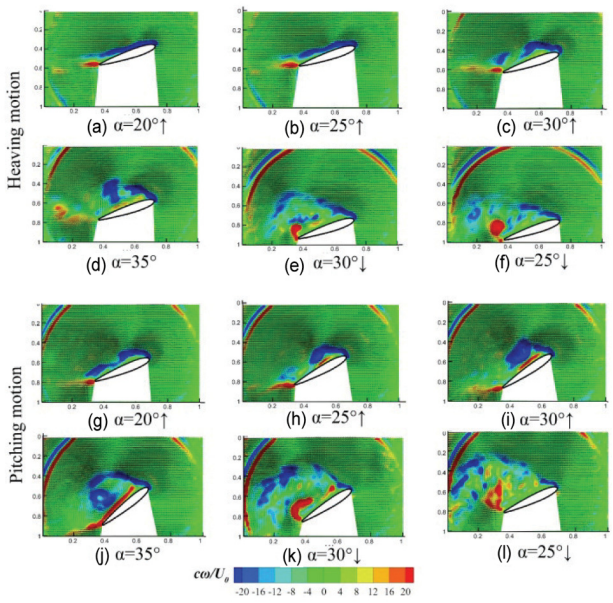

Fig. 10. Vorticity contours superimposed with velocity vectors at different angles of attack for case 4.

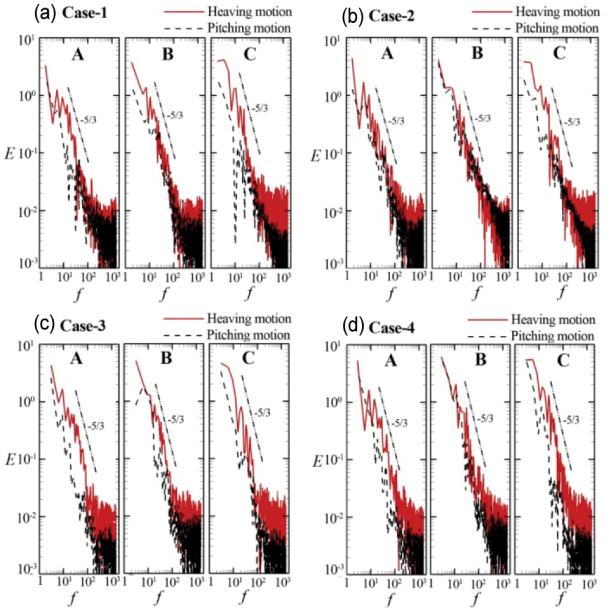

Fig. 11. Energy spectrum for three different points (A, B, and C) aligned vertically near the airfoil with regard to Fig. 2. The results are provided for both pure heaving and pure pitching motions for cases 1 to 4.

edge begins to develop and the LEV pinch-off occurs (Figs. 10(e) and (k)). The TEV strength for pure pitching motion seems to be higher than that of pure heaving motion at α = 30°, which indicates that the lift force for pure pitching motion is notably lower than that of pure heaving motion at the same angle. At α = 25°, the flow is strongly separated for both pure heaving and pure pitching motions (Figs. 10(f) and (l)), and in the post-stall region, the lift coefficient drops significantly. However, these results show that at higher reduced frequencies, the TEV for pure pitching motions is stronger than that of pure heaving motions, which means the lift reduction might be greater for these cases.

The overall results show that the flow structures are different for pure pitching and pure heaving motions. The pure heaving motion adds more kinetic energy to the boundary layer, which yields more stable flow over the suction side of the airfoil. Thus it decelerates the flow reversal and separation point movement. Therefore, more delay is expected in the stall for pure heaving motion as opposed to pure pitching motion. Regardless of kinematics, at a lower reduced frequencies (k = 0.25), dynamic stall can occur even before reaching the maximum angle of attack. However, at a higher reduced frequency (k = 0.375), the dynamic stall may occur even after the maximum angle of attack. This situation occurs when the kinematic motion provides adequate energy to the fluid-structure interactions, which adds more kinetic energy to the fluid around the airfoil. Therefore, in this case, dynamic stall occurs when the angle of attack is decreasing.

4.3 Turbulence

One of hypothesis on why kinematics influences the aerodynamics of the airfoil in deep dynamic stall condition is that the pure heaving motion adds extra kinetic energy to the boundary layer. As opposed to pure pitching motion, the extra energy comes from another velocity component derived from the pure heaving motion. However, to consider this hypothesis, the kinetic energy inside and in the vicinity of the boundary layer should be examined. To do so, the turbulence kinetic energy (here in 2D) was measured and turned into a spectrum using the fast Fourier transform (FFT).

Fig. 2 shows the locations for data acquisition to measure the turbulence kinetic energy. As the airfoil moves, the location of these three points varies with respect to the domain, but they are stationary with respect to the airfoil. The points are also located near the leading edge, where turbulence characteristics are more important to investigate. This idea increases the probability of measuring different ranges of turbulence scales with these three points. Fig. 11 shows the energy spectrum for points A, B, and C, as indicated in Fig. 2. The vertical axis represents the turbulence kinetic energy per unit mass, and the horizontal axis represents the turbulence frequency, f (Hz). Because the frame rate of the camera was set to 3000 fps, the maximum turbulence frequency that can be captured is 1500 Hz. As shown in Fig. 11(a), the maximum kinetic energy belongs to the pure heaving motion at the lowest frequencies. The turbulence kinetic energy for pure heaving motion in the inertial range is notably greater than that of pure pitching motion. In other words, the pure heaving motion leads to higher turbulence kinetic energy. This fact also adds extra energy to the boundary layer, which yields a delay in separation, and empowering of core vortices. Fig. 11(b) shows the energy spectrum for case 2. In this case, the pure heaving motion

seems to provide higher energy in the boundary layer than pure pitching motion. The energy spectra at point B seem to be similar for both pure heaving and pure pitching, but the pure heaving motion has higher energy in the inertial range. Fig. 11(c) shows the energy spectrum for case 3. The slope of the energy spectrum versus the turbulence frequency is the same for both pure heaving and pure pitching motions because the inertial range is universally independent. At higher frequencies, the noise increases because of the PIV measurement technique and the limited size of the interrogation cells. The size of the interrogation cells does not allow us to detect eddies smaller than the interrogation cells. Therefore, as the frequency increases, the results for such eddies appear as noise in the spectrum. Fig. 11(d) shows the energy spectrum for different points in case 4. The maximum energy for pure heaving motion is slightly high at points B and C, while the differences in the inertial subrange increase notably. Like in previous cases, the pure heaving motion produces higher turbulence kinetic energy than pure pitching motion. This extra energy decelerates the reversal flow and instability inside the boundary layer. The adverse pressure gradient is also delayed, which leads to a delay in the stall or stronger core vortices.

4.4 Decomposition of flow structure

In deep dynamic stall, the flow is highly unstable, and the turbulent flow is characterized by coherent structures that are often significant part of flow mechanisms. These coherent structures are large-scale vortices that are usually obscured by small-scale turbulent fluctuations [36]. By using the proper orthogonal decomposition (POD) approach, it is possible to identify the most energetic coherent structures in deep dynamic stall, and investigate their roles in the stall mechanism.

The POD of the velocity vector in the domain, $U = (u,v)$, has an orthonormal set of bases that are invariant with time. The POD modes represent the flow features that are orthonormal to each other [37] and are defined as follows:

$$\Phi_i = \left\{ \Phi_i^u, \Phi_i^v \right\}. \tag{9}$$

Each mode is related to a temporal coefficient $a_i(t)$, and the contribution from each flow feature to the original flow field is $a_i(t)\Phi_i$. The temporal coefficient $a_i(t)$ is the instantaneous weight of each flow feature at different moments of time [38]. After decomposition of the flow field, the original velocity field can be obtained from summation of the m modes [39]:

$$U = \sum_{i=0}^{m} a_i(t)\Phi_i(x,y). \tag{10}$$

The variance of temporal coefficients, $< a_i^2 >$, shows the contribution of each mode to the area-averaged mean kinetic energy, KE [39]. Hence, the modes can be ordered with respect to KE. The kinetic energy of the original flow field can be obtained by summation of the variance of temporal coefficients [40] as follows:

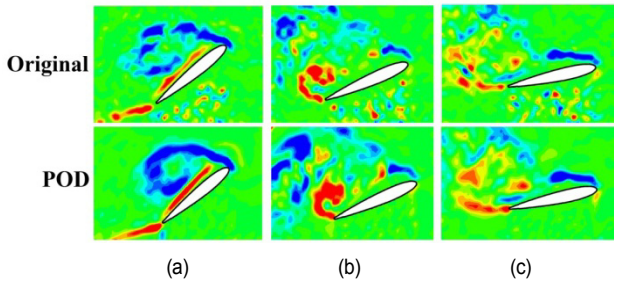

Fig. 12. Comparison of flow field for the original image and reconstructed one using POD.

$$KE_{total} = \sum_{i=0}^{m} \left\langle a_i^2 \right\rangle. \tag{11}$$

The flow in the PIV domain was decomposed, and the flow field was categorized into different modes. Fig. 12 illustrates the advantages of decomposition and reconstruction of the flow field using POD. Case 4 is selected because it has more complicated flow structure in the post-stall region. Fig. 12 shows the vorticity contours, and it compares the original and reconstructed flow fields using POD for the same sequences. In Fig. 12(a), the airfoil is around the stall point. In this moment the LEV is developed, and it almost covers the suction side of the airfoil. In the original image, the LEV is associated with small-scale structures or measurement errors. There are also numerous sharp values on the pressure side of the airfoil in the shadow region, which is noise from the PIV and post-processing calculations. In the POD image, the results are reconstructed for only the first 20 energetic modes. The noise on the pressure side of the airfoil is dampened and removed from the flow field. In Fig. 12(b), the TEV is growing and rolling up after the LEV pinch-off. In the original image, the TEV is dispersed. Additionally, the wake has large-scale vortices containing numerous eddies. However, in the reconstructed image, the TEV has more solidarity, and the wake is recovered by its coherent structures. By reducing the angle of attack in the post-stall region (Fig. 12(c)), the noise on the pressure side of the airfoil increases in the original image, and the wake has no integrity due to small-scale vortices. But in the reconstructed image, the wake has more integrity, and even during massive flow separation, there is still a sign of large-scale structures. Therefore, by using the POD approach, it is possible to identify large-scale and energetic structures.

Figs. 13 and 14 are also provided to investigate different flow modes. The energy bars show the amount of kinetic energy in each mode as the percentage of the mean kinetic energy. The cumulative energy also represents the amount of total energy. We provided only 20 modes to examine the flow characteristics. As shown in Figs. 13(a) and (b), the first mode in pure heaving motion contains 50 % of the total energy, while the first mode in pure pitching motion contains only 32 % of total energy. For the

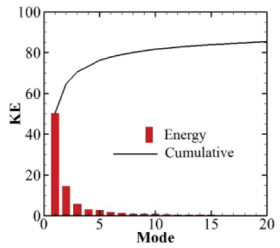

(a) Heaving motion, case-1

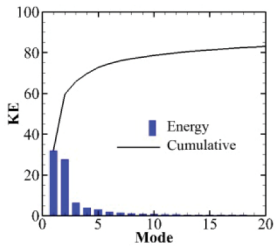

(b) Pitching motion, case-1

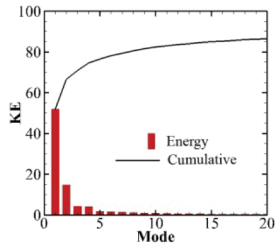

(c) Heaving motion, case-2

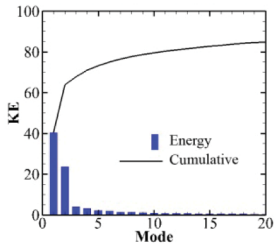

(d) Pitching motion, case-2

Fig. 13. Kinetic energy for the first 20 decomposed modes for cases 1 and 2. The energy bar shows the percentage of kinetic energy with respect to the total energy of fluid. The cumulative energy shows the summation of energies for a group of modes.

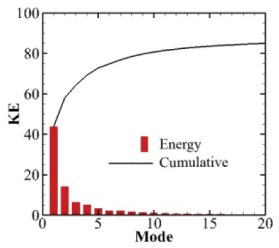

(a) Heaving motion, case-3

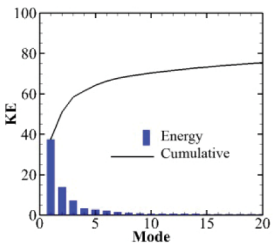

(b) Pitching motion, case-3

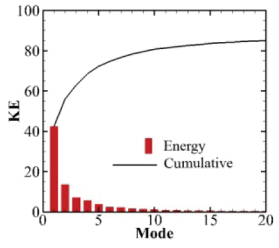

(c) Heaving motion, case-4

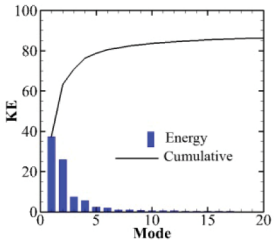

(d) Pitching motion, case-4

Fig. 14. Kinetic energy for first 20 decomposed modes for cases 3 and 4. The energy bar shows the percentage of kinetic energy with respect to the total energy of the fluid. The cumulative energy shows the summation of energies for a group of modes.

pure heaving motion the second mode has 14 % of the total energy, while for pure pitching motion the second mode contains 23 %. The rest of the modes may each contain 5 % of total energy or less. The cumulative energy for pure heaving and pure pitching motions for the two primary modes are 64 % and 58 %, respectively. This means that regardless of kinematics, the first and second modes are dominant structures in the flow field. Figs. 13(c) and (d) show the flow reconstruction for case 2, in which the energy of the first and second modes for pure heaving motion is 52 % and 18 %, respectively. For the pure pitching motion, these values are 40 % and 23 %, respectively. The cumulative for both pure heaving and pure pitching motions are more than 60 %. With an increase in the number of modes, the rate of change for the cumulative energy decreases notably, and the total energy reaches more than 80 %. In other words, 80 % of the total energy occurs with the first twenty modes, while the primary modes are more dominant in the flow structure.

In cases 1 and 2, the first mode for pure heaving motion contains more energy than that of pure pitching motion, while the second mode contains less energy than that of pure pitching motion. In other words, in pure pitching motion, the energy is more highly distributed among other modes in comparison to pure heaving motion. This indicates that the first mode in pure heaving motion is dominant in the flow field, which indicates solidarity of the flow structure during the dynamic stall process.

Fig. 14 shows the kinetic energy of the first 20 modes for cases 3 and 4. As shown in Figs. 14(a) and (b), the kinetic energy for the first and second modes for pure heaving motion are 43 % and 14 %, respectively. These amounts for pure pitching motion are 37 % and 14 %, respectively. The rest of the modes for both pure heaving and pure pitching motions have less than 7 % kinetic energy. In this case, the first mode for pure heaving motion contains more kinetic energy than that of pure pitching motion. As shown in Figs. 14(c) and (d), the first and second modes for pure heaving motion have 42 % and 14 % of total kinetic energy, respectively. These values for pure pitching motion are 37 % and 25 %, respectively. The rate of change in the cumulative energy for pure heaving motion is less than that of pure pitching motions. This is because the first mode in pure heaving motion contains higher kinetic energy, which can be considered as the dominant mode in the flow structure during dynamic stall. Again, in cases 3 and 4, the flow structure for pure heaving motion has more solidarity, and the coherent structures could be more stable in comparison to the pure pitching motion.

At the end, the POD results show greater solidarity of coherent structures for pure heaving motion compared to pure pitching motion. This indicates that the kinetic energy increases in the shear, boundary, and mixing layers, which makes the flow more stable. It also enhances the solidarity of coherent structures during dynamic stall.

5. Conclusions

In this study, the deep dynamic stall of a NACA 0012 was experimentally investigated for pure heaving and pure pitching experimentally. To visualize the flow structure over the moving airfoil, a time-resolved PIV method was applied. The aerodynamic loads were computed using a control-volume approach. Additionally, the flow filed was decomposed into different modes and reconstructed using POD. After decomposition, the

pure heaving motion has a high-energy mode. This mode makes the flow structure more stable in deep dynamic stall conditions, in contrast to pure pitching motions.

The turbulence in the flow field was also measured at three different points aligned vertically near the moving airfoil. The turbulence in the boundary, shear, and mixing layers increases due to excessive kinetic energy produced by pure heaving motion. The high energy in boundary layer makes the flow more stable. Hence, the flow reversal decelerates, and the transfer of the separation point toward the leading edge is postponed for pure heaving motion.

In the case of aerodynamic loads, at lower angles of attack in the pre-stall region, the pure pitching motion produces higher lift force than pure heaving motion. Furthermore, when the LEV is created, the pure heaving motion has stronger core vortices, and it produces a higher lift peak. In the post-stall region, the lift force for pure heaving motion is usually more stable than that of pure pitching motion. Additionally, the drag force for pure pitching motion is usually higher than that of pure heaving motion. Finally, this study shows that the kinematics may change the flow structure, and hence, the aerodynamic loads during deep dynamic stall conditions. Therefore, corresponding kinematics should be determined first, and based on the related motion, the dynamic stall should be considered.

Acknowledgments

This research was supported by the National High-end Foreign Experts Recruitment Plan of China (No. G20190023036). This study was also supported by the National Research Foundation of Korea (NRF) grant, which is funded by the Korean government (MSIT) (No. 2011-0030013, No. 2018R1A2 B2007117).

References

[1] Y. Kim and Z.-T. Xie, Modelling the effect of freestream turbulence on dynamic stall of wind turbine blades, *Computers & Fluids*, 129 (2016) 53-66.

[2] J. M. Yu, T. S. Leu and J. J. Miau, Investigation of reduced frequency and freestream turbulence effects on dynamic stall of a pitching airfoil, *Journal of Visualization,* 20 (2017) 31-44.

[3] L. Siegel, K. Ehrenfried, C. Wagner, K. Mullenners and A. Henning, Cross-correlation analysis of synchronized PIV and microphone measurements of an oscillating airfoil, *Journal of Visualization,* 21 (2018) 381-395.

[4] K. Gharali and D. A. Johnson, Effects of nonuniform incident velocity on a dynamic wind turbine airfoil, *Wind Energy*, 18 (2015) 237-251.

[5] H. R. Karbasian, J. A. Esfahani and E. Barati, Effect of acceleration on dynamic stall of airfoil in unsteady operating conditions, *Wind Energy*, 19 (2016) 17-33.

[6] H. Hirano et al., Smoke-wire flow visualization of the dynamic stall vortex over the basic wing-body model in pitching motion, *Journal of Visualization,* 3 (2001) 311.

[7] M. R. Amiralaei, H. Alighanbari and S. M. Hashemi, Flow field characteristics study of a flapping airfoil using computational fluid dynamics, *Journal of Fluids and Structures*, 27 (2011) 1068-1085.

[8] P. Gerontakos and T. Lee, PIV study of flow around unsteady airfoil with dynamic trailing-edge flap deflection, *Experiments in Fluids*, 45 (2008) 955.

[9] K. Gharali and D. A. Johnson, Dynamic stall simulation of a pitching airfoil under unsteady freestream velocity, *Journal of Fluids and Structures,* 42 (2013) 228-244.

[10] H. R. Karbasian and K. C. Kim, Numerical investigations on flow structure and behavior of vortices in the dynamic stall of an oscillating pitching hydrofoil, *Ocean Engineering*, 127 (2016) 200-211.

[11] T. Lee and P. Gerontakos, Investigation of flow over an oscillating airfoil, *Journal of Fluid Mechanics*, 512 (2004) 313-341.

[12] M. Masdari, M. Seyednia and A. Tabrizian, An experimental loading study of a pitching wind turbine airfoil in near- and post-stall regions, *Journal of Mechanical Science and Technology,* 32 (8) (2018) 3699-3706.

[13] W. J. McCroskey, Unsteady airfoils, *Annual Review of Fluid Mechanics*, 14 (1982) 285-311.

[14] M. N. Sefiddashti, M. Nili-Ahmadabadi and B. S. Rizi, Experimental study of effects of circular-cross-section riblets on the aerodynamic performance of Risø airfoil at transient flow regime, *Journal of Mechanical Science and Technology,* 32 (2) (2018) 709-716.

[15] M. M. Koochesfahani, Vortical patterns in the wake of an oscillating airfoil, *AIAA Journal*, 27 (1989) 1200-1205.

[16] K. D. Jones, C. M. Dohring and M. F. Platzer, Experimental and computational investigation of the Knoller-Betz effect, *AIAA Journal*, 36 (1998) 1240-1246.

[17] J. Young and J. C. S. Lai, Oscillation frequency and amplitude effects on the wake of a plunging airfoil, *AIAA Journal,* 42 (2004) 2042-2052.

[18] J. Zhu and J. Zhang, Power extraction performance of two semi-active flapping airfoils at biplane configuration, *Journal of Mechanical Science and Technology,* 34 (1) (2020) 175-187.

[19] J. M. Anderson, K. Streitlien, D. S. Barrett and M. S. Triantafyllou, Oscillating foils of high propulsive efficiency, *Journal of Fluid Mechanics*, 360 (1998) 41-72.

[20] M. A. Ashraf, J. Young and J. C. S. Lai, Reynolds number, thickness and camber effects on flapping airfoil propulsion, *Journal of Fluids and Structures*, 27 (2011) 145-160.

[21] A. R. Shanmugam and C. H. Sohn, Numerical investigation on thrust production and unsteady mechanisms of three-dimensional oscillating wing, *Journal of Mechanical Science and Technology,* 33 (12) (2019) 5889-5900.

[22] J. A. Esfahani, E. Barati and H. R. Karbasian, Fluid structures of flapping airfoil with elliptical motion trajectory, *Computers & Fluids*, 108 (2015) 142-55.

[23] Y. Gao, Q. Zhu and L. Wang, Measurement of unsteady transition on a pitching airfoil using dynamic pressure sensors, *Journal of Mechanical Science and Technology,* 30 (10) (2016)

4571-4578.
[24] J. A. Esfahani, H. R. Karbasian and E. Barati, Proposed kinematic model for fish-like swimming with two pitch motions, *Ocean Engineering*, 104 (2015) 319-328.
[25] A. R. Shanmugam and C. H. Sohn, Numerical investigation of the aerodynamic benefits of wing-wing interactions in a dragonfly-like flapping wing, *Journal of Mechanical Science and Technology,* 33 (6) (2019) 2725-2735.
[26] D. A. Read, F. S. Hover and M. S. Triantafyllou, Forces on oscillating foils for propulsion and maneuvering, *Journal of Fluids and Structures*, 17 (2003) 163-183.
[27] G. Cao et al., Nonlinear dynamic response of cable-suspended systems under swinging and heaving motion, *Journal of Mechanical Science and Technology,* 31 (7) (2017) 3157-3170.
[28] H. R. Karbasian, J. A. Esfahani and E. Barati, The power extraction by flapping foil hydrokinetic turbine in swing arm mode, *Renewable Energy*, 88 (2016) 130-142.
[29] Y. M. Koo et al., Practical payload assessment of a prototype blade for agricultural unmanned rotorcraft, *Journal of Mechanical Science and Technology,* 32 (12) (2018) 5659-5669.
[30] A. Tagliabue, S. Scharnowski and C. J. Kähler, Surface pressure determination: A comparison between PIV-based methods and PSP measurements, *Journal of Visualization,* 20 (2017) 581-590.
[31] M. Radmanesh, M. Nili-Ahmadabadi, O. Nematollahi and K. C. Kim, Experimental study of square riblets effects on delta wing using smoke visualization and force measurement, *Journal of Visualization,* 21 (3) (2018) 421-432.
[32] B. W. van Oudheusden, F. Scarano, E. W. M. Roosenboom, E. W. F. Casimiri and L. J. Souverein, Evaluation of integral forces and pressure fields from planar velocimetry data for incompressible and compressible flows, *Experiments in Fluids,* 43 (2007) 153-162.
[33] K. Gharali and D. A. Johnson, PIV-based load investigation in dynamic stall for different reduced frequencies, *Experiments in Fluids*, 55 (2014) 1803.
[34] S. Wang, D. B. Ingham, L. Ma, M. Pourkashanian and Z. Tao, Turbulence modeling of deep dynamic stall at relatively low Reynolds number, *Journal of Fluids and Structures*, 33 (2012) 191-209.
[35] T. Durhasan and İ. Karasu, Dye visualization over double delta wing with various kink angles, *Journal of Visualization,* 22 (4) (2019) 669-681.
[36] S. H. Kim and H. D. Kim, Quantitative visualization of the three-dimensional flow structures of a sweeping jet, *Journal of Visualization,* 22 (3) (2019) 437-447.
[37] G. Berkooz, P. Holmes and J. L. Lumley, The proper orthogonal decomposition in the analysis of turbulent flows, *Annual Review of Fluid Mechanics*, 25 (1993) 539-575.
[38] D. Gil-Prieto, D. G. MacManus, P. K. Zachos, G. Tanguy, F. Wilson and N. Chiereghin, Delayed detached-eddy simulation and particle image velocimetry investigation of S-duct flow distortion, *AIAA Journal*, 55 (2017) 1893-1908.
[39] J. L. Lumley, *Stochastic Tools in Turbulence*, New York: Dover (2007).
[40] L. Sirovich, Turbulence and the dynamics of coherent structures, Part 1: Coherent structures, *Quarterly of Applied Mathematics,* 45 (1987) 561-571.

Gul Chang is a Ph.D. student at Pusan National University, Korea. His main research interest is thermo-fluid dynamics in air conditioner and heat exchanger. He is currently working at the R&D Lab. of the Air Solution Division, LG Electronics, Korea.

Hamid Reza Karbasian is a M.Sc. student in School of Mechanical Engineering in Pusan National University. His main research interest is application of fluid mechanics in aerospace and energy conversion systems. He is currently working on flow measurements and flow instabilities in wind energy division.

Shujun Zhang is an Associate Professor of China Aerodynamics Research and Development Center. He received his master and Ph.D. degrees from National University of Defense Technology in 2002 and 2006, respectively. His major research interests are computational aerodynamics, aeroelasticity, and multi-disciplinary integrated design of aircraft.

Yao Yan is an Associate Professor of the School of Aeronautics and Astronautics, University of Electronics Science and Technology of China. He obtained his Ph.D. in Mechanics in 2014 from Tongji University, Shanghai, China. His research interests include regenerative cutting chatter and control for suppression, vibro-impact capsule robot, control of multistability, and exoskeleton robot.

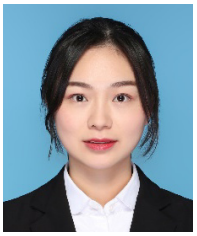

Binqi Chen is a Lecturer of the School of Aeronautics and Astronautics, University of Electronics Science and Technology of China. She obtained her Ph.D. in Aircraft Design in 2016 from Nanjing University of Aeronautics and Astronautics, Nanjing, China. Her research interests include intelligent unmanned aerial vehicle technology and multi-disciplinary optimization of aircraft.

Kyung Chun Kim is a Distinguished Professor at the School of Mechanical Engineering of Pusan National University in Korea. He obtained his Ph.D. from the Korea Advanced Institute of Science and Technology (KAIST), Korea, in 1987. He was selected as a Member of the National Academy of Engineering of Korea in 2004. His research interests include flow measurements based on PIV/LIF, POCT development, wind turbines, and organic Rankine cycle system.